Geomechanics and Engineering, *Vol. 36, No. 5 (2024) 475-487*
https://doi.org/10.12989/gae.2024.36.5.475

A new viewpoint on stability theorem for engineering structural and geotechnical parameter

Timothy Chen[1,2], Ruei-Yuan Wang[**1], Yahui Meng[1] and Z.Y. Chen[*1]

[1]*Guangdong University of Petrochem Technol, Sch Sci, Maoming City, Kuan-Du Avenue, No. 139, Peoples R China 525000*
[2]*Division of Eng App Sci, Caltech, CA 91125, USA*

(*Received January 3, 2023, Revised October 13, 2023, Accepted February 19, 2024*)

Abstract. Many uncertainties affect the stability assessment of rock structures. Some of these factors significantly influence technology decisions. Some of these factors belong to the geological domain, and spatial uncertainty measurements are useful for structural stability analysis. This paper presents an integrated approach to study the stability of rock structures, including spatial factors. This study models two main components: discrete structures (fault zones) and well known geotechnical parameters (rock quality indicators). The geostatistical modeling criterion are used to quantify geographic uncertainty by producing simulated maps and RQD values for multiple equally likely error regions. Slope stability theorem would be demonstrated by modeling local failure zones and RQDs. The approach proided is validated and finally, the slope stability analysis method and fuzzy Laypunov criterion are applied to mining projects with limited measurement data. The goals of this paper are towards access to adequate, safe and affordable housing and basic services, promotion of inclusive and sustainable urbanization and participation, implementation of sustainable and disaster-resilient buildings, sustainable human settlement planning and manage. Simulation results of linear and nonlinear structures show that the proposed method is able to identify structural parameters and their changes due to damage and unknown excitations. Therefore, the goal is believed to achieved in the near future by the ongoing development of AI and fuzzy theory.

Keywords: artificial intelligence; fuzzy models; geology; geostatic simulation; slope resistance; uncertainty

1. Introduction

The geological characteristics of the rock mass are important factors in the structural engineering stability of the ideal open pit mine systems. Understanding geomechanical characteristics can magnificently improve our knowledge of the role of rock behavior in reducing the dangers of slope failure in the open mining operations. Structural stability is a key factor in rock structure field and during the slope stabilization project, boreholes were installed in various parts of the site to improve site surveys. Johari (2023) combined geostatistics and finite element methods to consider the location of known data through conditional spatial variations in soil characteristics. The system reliability index is smaller than all other indices, indicating that analyzes performed without considering the known material locations provide a reliability index that is more reliable than the true value.

Traditionally, deposits are divided into geotechnical zones, creating specific boundary patterns based on the geometric, geotechnical and structural structures present in the study area (Ronaldo *et al.* 2019, Zhang *et al*. 2023, 2024). Fixed values for the geomechanical characteristics of each geotechnical zone are determined by averaging all relevant data for that zone. In particular, scale of variation is used to evaluate the correlation between geotechnical parameters of two locations. This is of great importance for mineral exploration and engineering. Chen *et al*. (2023) first estimated the performance of the conventional moment method and then selected the exponential autocorrelation function method, which has the best SOF estimation performance, to improve the accuracy of estimating the scale of variation in rock characteristics around the tunnel. Recently, researchers have begun to use geostatic modeling techniques to describe heterogeneity in geometric characteristics (Silvestre *et al.* 2002, Prasanth *et al*. 2007).

Geostatistical methods are more useful because they calculate mathematical models of the stochastic and structural characteristics of variables. However, the uncertainties associated with using geostatistics to model spatial heterogeneity in geometric characteristics must be carefully considered.

Although it is easy to measure soil and rock characteristics in the laboratory, it is difficult to know how representative a small sample is of a large rock mass. Traditionally, slopes have been evaluated based on factors of safety. Uncertainties related to mechanical characteristics, geology, environmental status, rock failure mechanisms, molecule pore pressures, and loading under safety strategies (Kim 2015, Yin *et al*. 2023, Tie *et al.* 2023, Wang *et al.* 2024). When analyzing the stability of exposed slopes, a risk analysis focusing only on the uncertainty of the geometric characteristics is required. Traditional slope stability analysis does not quantitatively consider the uncertainty of geometric characteristics. To estimate this

*Corresponding author
E-mail: t13929751005@gmail.com
**Corresponding author
E-mail: rueiyuan@gmail.com

ISSN: 2005-307X (Print), 2092-6219 (Online)

uncertainty, probabilistic methods of calculating safety factors are preferred over traditional slope stability analysis (Camp *et al.* 2022). There are also uncertainties about the methods used to assess the severity of defects in recent decades. The probabilistic slope stabilization method calculates the general distribution of reliability coefficients based on random input variables with certain statistical characteristics (Naik and Singh 2007). The probability of failure is determined by the distribution of safety factor values. However, analytical calculations of safety distribution factors using this method are systematically inefficient according to simulation-based algorithms. Similar to Monte Carlo simulations, the distribution of slope safety factors can be estimated.

Although Monte Carlo theory has been applied to analyze slope stability, past studies have ignored the spatial rock heterogeneity of geometric characteristics when calculating safety uncertainty factors. Geological formations have a decisive influence on the stability of slopes and must be taken into account while deriving and operating slope stability analysis on these criterion of rocks.

Test drilling is subject to economic, environmental and technical constraints. It is impossible to cover all the interesting places in the area. The use of non-statistical methods to model geomechanical parameters from sample values measured in rock masses overcomes these limitations. Geological feature interpolation uses two general modeling approaches: stochastic and deterministic.

The process of modeling fault networks is full of uncertainties because it is limited by survey data and existing interpretation methods. In hydrogeological engineering, fracture location uncertainty plays an important role in decision-making and project safety. However, with traditional uncertainty modeling techniques, it is difficult to obtain accurate uncertainty quantification and topological representation. To achieve this objective, Han *et al*. (2022) proposed a new solution for uncertainty analysis and 3D fault modeling using deep learning techniques. The simulations produced maps showing regional variations and heterogeneity in rock mass parameters that were not possible with previous estimation methods. Compared to analytical methods, simulations are more sensitive to significant patterns showing very high and very low scores. Finally, slope stability was analyzed using geological model maps as input to the model. Slope stability theory and analysis is a possible application of geological modeling.

In this paper, we present a method for assessing the stability of exposed slopes with uncertain geological, engineering structural and soil variables. Uncertainties or measurements are quantified using geostatistical modeling algorithms that combine classification (geological structures) and continuity (geotechnical parameters). The proposed method was validated with synthetic materials and applied to an open-pit-site field mine. Geotechnical information on this deposit is limited. Therefore, our demonstration focuses on robustness analysis using limited data. However, the proposed method can be applied to many soil parameters. This paper models structural, fault and rock quality (RQD) parameters, which are the only parameters available for study. RQD is the proportion of objects with a total core length greater than 10 cm. The quality is divided into five grades: very poor (0% -25%), poor (25% - 50%), normal (50%-75%), and good (75% - 90%) and excellent (90% < RQD 100%). The friction and cohesion components of the five RQDs correspond to the five RQD values. They include (1) using closed rock surfaces and (2) using caution with predicted values of friction components in isotropic framworks. Although this method is an indirect method of calculating the friction coefficient and cohesion coefficient, it is effective and simple when these values cannot be measured directly. The safety factor is used to estimate the uncertainty of closed cell structures and calculate reliability. The value of the safety factor is calculated according to the target balance method. Model the geological structure and geometric characteristics of potential open areas using limited data.

This method takes into account spatial uncertainties in geological structures and geotechnical parameters and can also be applied to rock tunnels, boreholes or other projects where there is an interest in assessing rock stability or strength in remote areas where data are limited.

2. Theoretical model of rock structure system

The proposed stability approach is divided into two distinct parts: (a) geographical modeling of engineering structural parameters and soil parameters; (b) analysis of slope stability and quantification of slope uncertainty using the limit equilibrium method.

2.1.1 Modeling geological structures using model indicators

Geological structures such as faults have a significant impact on mining and engineering. The tensile strength of the fault zone is significantly lower than the strength of the surrounding rock mass. Fault zone (i.e., fault/fault) information obtained from core logs can help generate fault zone maps of proposed deposits. Estimating the error map using traditional interpolation numerical algorithms such as kriging generates a smooth continuous map. Data variability is underestimated. Simulation-based methods overcome the limitations of interpolation. In the simulation, each individual research area is treated as an arbitrary variable. In the error model, Z(u) is a the categorical RV that takes one of the two k values if the error is at position u, otherwise it is 0 (Kim 2021, Jo 2018 Kim 2019, Lihorn 2022 and Yu 2020).

Lemma 1 (Wang *et al.* 1996): The equilibrium point of fuzzy criterion in an arbitrary nonlinear system is asymptotically stable in the large if there exists a common positive definite matrix P such that

$$A_i^T P A_i - P < 0, \text{ for } i = 1, 2, \cdots, r.$$

The probability density at position u of the conditional function is calculated as follows (Katelyn 2020, Jori 2023)

$$f(u;k|(n)) = Prob\{Z(u) \in category\, k|(n)\} \quad (1)$$

where $|(n)$ represents the position of adjacent data values.

To obtain the probability density function in the Eq. (1),

the error profile $Z(u)$ is switched to a binary index using a replaced function defined as

$$I(u;k)=\begin{cases}1, if\ Z(u)\in k\\ 0, otherwise\end{cases} \tag{2}$$

The obtained probability density function at the unknown position u is calculated based on the weighted average of the error information of adjacent transformation indexes. Calculate the weights by solving the Kriging equation. To account for the error data produced by solving the kriging equation, a spatial variogram model was created. Taylor series modeling Eq. (3) is used to calculate the experimental covariance of the index error data and convert it into binary index data.

$$\gamma_I(h;k)=\frac{1}{2N(h)}\sum_{a=1}^{N(h)}\left[z(u_a;k)-z(u_a+h;k)\right]^2$$
$$f_n(x):=\sum_{i=0}^{n-1}\frac{f^{[i]}(0)}{(i)!}x^i \tag{3}$$

Assume $f0(x)=0$ (the positive number passes through the origin), let

$$T_n(x):=\frac{f(x)-f_n(x)}{x^n}=\frac{f^{[n]}(\psi(x))}{n!}$$

among them

$$\mu(x):=\frac{T_n(x)-\psi_2}{\psi_1-\psi_2}$$

So at this time it can be expressed as$f(x)=f_n(x)+T_n(x)x^n$

$$f(x)=f_n(x)+(\mu(x)\psi_1+(1-\mu(x))\psi_2)x^n$$

From the results of the above formula, we can get that P1 and P2 in formula (3.1) are

$$P_1=f_n(x)+\psi_1x^n$$
$$P_2=f_n(x)+\psi_2x^n.$$

Example: Consider a sinusoidal Taylor series curve

$$\sin(x)=x-\frac{x^3}{3!}+\frac{x^5}{5!}-\frac{x^7}{7!}+\cdots$$

From formula (3)

The linear term sine wave in Taylor series can be defined as

$$f_1=0, T_1(x)=\frac{\sin(x)-0}{x}$$

The maximum value in the range $\sin(x)/x$-1,1] is 1 and the minimum value is 0.8415, which can be expressed as

$$\sin(x)=\mu_1(0+1x)+\mu_2(0+0.8415x).$$

of can be expressed as

$$f_3=0+x, T_3(x)=\frac{\sin(x)-x}{x^3}$$

After calculation, the maximum value in the interval $[-1,1]$ is -0.1585 $T_3(x)$and the minimum value is -0.1667. it might work

$$\sin(x)=x+\mu_1(0-0.1585x^3)+\mu_2(0-0.1667x^3).$$

The Taylor series sinusoid of the fifth term can be expressed as

$$f_5=0+x-\frac{x^3}{6}, T_5(x)=\frac{\sin(x)-x+x^3/6}{x^5}$$

After calculation, the maximum value in the interval [$T_5(x)-1,1$] is 0.0083336, and the minimum value is 0.0081376, we can get

$$\sin(x)=x-\frac{x^3}{6}+(\mu_1 0.0083336x^5+\mu_2 0.0081376x^5)$$

Similarly, the example simulations will use the linear system from this section.

2.1.2 Modeling soil parameters through sequential Gaussian modeling

After the calculation of the model geological structure is completed, the soil parameters of each index are modeled in the model structure diagram. We note here that only one geotechnical parameter, RQD, is available in the exploration mine. This article will use the finite element method to deal with differential equations and integral equations. In order to maintain numerical stability during the process of solving discontinuous boundary conditions, we use ABAQUS to subdivide large physical systems into tiny parts, which is to discretize the continuous system., divide the model into discretized blocks and analyze the interaction between each block to calculate the physical behavior of the model. If we set the grid size smaller, the calculation results will be more accurate but the calculation time will also increase significantly. The grid size should be adjusted within the acceptable numerical error range.

A complete ABAQUS consists of three parts. The flow chart is shown in Fig. 1. The first part is the pre-processing part. At this stage, ABAQUS/CAE is used to create the model's dimensions, material characteristics, elements, output data and other settings. It can also be used through a compatible third party. The CAD software converts the geometric model into an ABAQUS/CAE compatible model through conversion processing. The second part is to submit the analysis calculation process using ABAQUS/Standard or ABAQUS/Explicit. The analysis module is suitable for processing linear and nonlinear problems. ABAQUS/Explicit is a special-purpose analysis module suitable for analyzing short-term or instantaneous problems. dynamic events. This study uses ABAQUS/Standard to perform analytical operations. The third part is the post-processing part. This stage is to organize the data, images and animations output after the second part of the operation and present them visually with 3D color rendering.

Normal point-wise transformations preserve the order of data samples and allow a simple inverse transformation. Variograms are calculated based on standardized RQD values. RQD modeling was performed as usual using simple kriging. When you perform a simulation at an unknown or uncertain location in the mine, the results are converted back to the given RQD data space.

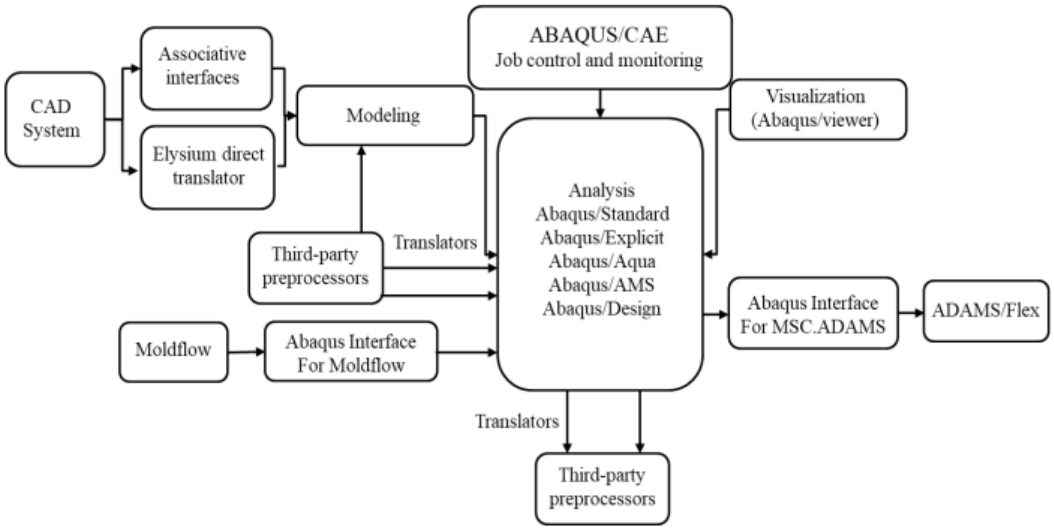

Fig. 1 Flow chart for rock structural analysis

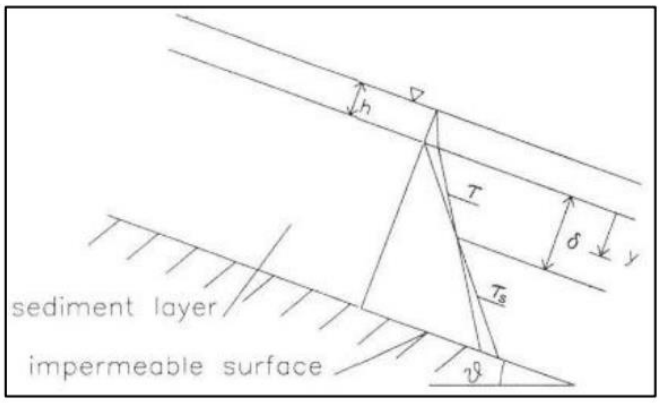

Fig. 2 Shows the forces acting on a typical plate

The calculating steps for stability are summarized below

Given a polynomial matrix$F(x) \in S^2$

$$F(x) = \begin{bmatrix} x^2 - 2x + 2 & x \\ x & x^2 \end{bmatrix}$$

From the definition, we can determine $F(x)$whether it is a square sum matrix

$$v^T F(x) v = \begin{bmatrix} v_1 \\ v_2 \end{bmatrix}^T \begin{bmatrix} x^2 - 2x + 2 & x \\ x & x^2 \end{bmatrix} \begin{bmatrix} v_1 \\ v_2 \end{bmatrix}$$

$$= \begin{bmatrix} v_1 \\ xv_1 \\ v_2 \\ xv_2 \end{bmatrix}^T \begin{bmatrix} 2 & -1 & 0 & 1 \\ -1 & 1 & 0 & 0 \\ 0 & 0 & 0 & 0 \\ 1 & 0 & 0 & 1 \end{bmatrix} \begin{bmatrix} v_1 \\ xv_1 \\ v_2 \\ xv_2 \end{bmatrix}$$

$$= \begin{bmatrix} v_1 \\ xv_1 \\ v_2 \\ xv_2 \end{bmatrix}^T \begin{bmatrix} 1 & 0 & 0 & 1 \\ -1 & 1 & 0 & 0 \end{bmatrix}^T \begin{bmatrix} 1 & 0 & 0 & 1 \\ -1 & 1 & 0 & 0 \end{bmatrix} \begin{bmatrix} v_1 \\ xv_1 \\ v_2 \\ xv_2 \end{bmatrix}$$

$$= (v_1 + xv_2)^2 + (xv_1 - v_1)^2$$

So this matrix is $F(x)$a sum of squares matrix. It should be noted that the Q matrix is not unique.

Symmetric relationships are also derived from the sum of squares method, as will be illustrated below. Let us consider a system

$$\dot{x} = Ax$$

Let it be a quadratic Lyapunov function

$$V(x) = x^T P x$$

The rate of change of its function over time is

$$\begin{aligned} \dot{V}(s) &= \dot{x}^T P x + x^T P \dot{x} \\ &= x^T (A^T P + PA) x \end{aligned}$$

Therefore, the conditions for finding the sum of squares can be obtained as follows

$$\begin{aligned} v^T (P - \epsilon_1) v &\quad \text{isSOS} \\ -v^T (A^T P + PA + \epsilon_2) v &\quad \text{isSOS} \end{aligned}$$

where v is any combination of vectors. After multiplying the left and right sides , the condition for finding the sum of squares is a scalar quantity. Since the sum of squares method inserts the vector vi into the matrix, it becomes a scalar and is calculated. The scalar will have the following ratio

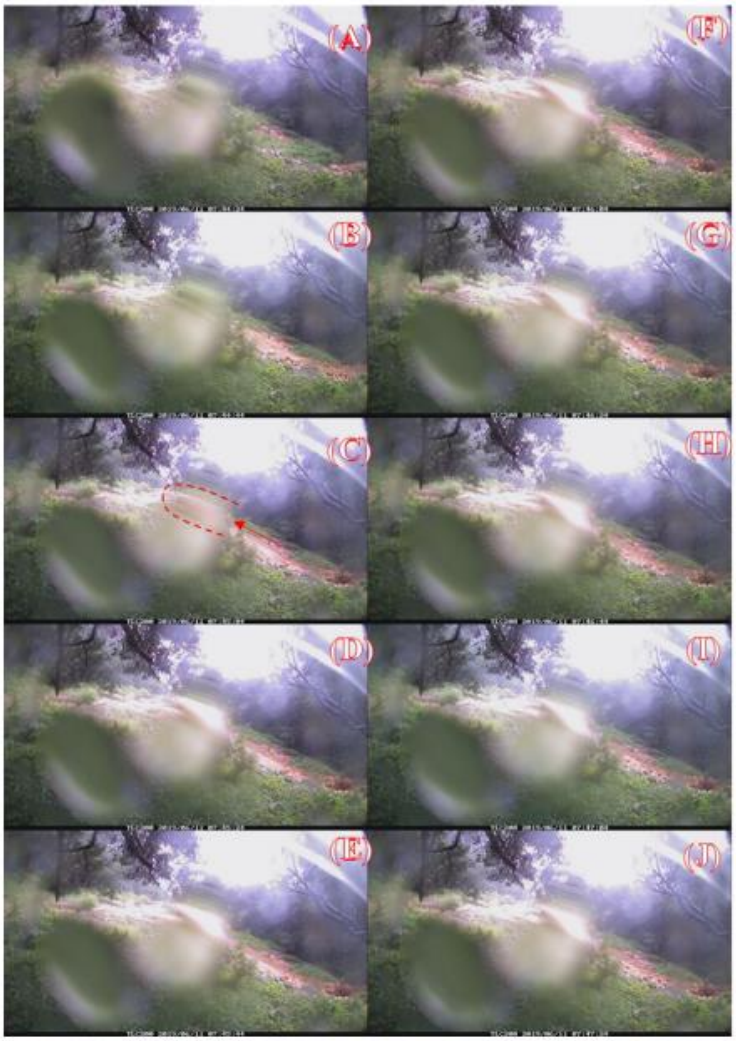

Fig. 3 Comparison of different categories of rock structure analysis

$$-v^T(A^TP + PA)v = -2v^T(A^TP)v = -2v^T(PA)v$$

It should be noted here that the researchers are aware of the limitations of this specific method. However, this method was chosen because of its computational efficiency. When looking for safe values, consider the forces acting on a typical disk (see Fig. 2). Using the limit equilibrium method and the parameters defined in Fig. 2, the safety factor F is calculated as follows

$$F= \text{tanpc'bseca+[1/cosa][W.cosp+ Qcosp] tan}\phi \,/\, \Sigma\,(W+WcosB+Qcosp)sina\ (wsin\beta+Qsinp)(cosa-h/k) \quad (4)$$

The standard cutting method is considered the simplest cutting method. This method assumes that the intermediate force is parallel to the base of each disc, giving a simple safety factor. Therefore, Bishop's method ignores lateral forces and only considers normal forces. An error-tried method is utilized to estimate the safety factor, which makes the analysis computationally efficient. Calculation of slope weight and safety factor based on error model and RQD model. In order to quantify the uncertainty in slope stability, it is necessary to determine safety factors for all combinations of failure modes and RQDs.

P*Q and RQD plots from a geological model developed to quantify uncertainty in fault zones were used to calculate slope and safety factors using the Bishop method. To quantify the well compaction uncertainty, the sum of safety factors P*Q can be determined. To calculate the probability of failure, P*Q numbers are generated from the map regardless of the scale type. For each simulation diagram, calculate the safety slope factor and safety factor Fs. The average value ðμFÞ is calculated as follows

$$\psi = 1/P^*Q(\Sigma F_i) \quad (5)$$

Calculated safety factor i and cartographic modeling of geological structures and soil parameters using the central limit theorem, the error probability of the proposed uncertainty-based slope model is calculated as follows

$$P_F = n_F/PQ \quad (6)$$

Where n_F is a function defined as
I(Fi)=1 or 0

The following is an overview of the steps to determine uncertainty in a slope stability analysis:

Table 1 Safety factors calculated from total data, as well as minimum, maximum and average safety factors calculated by simulation

slope(°)	Exhaustive Dataset's (Q/min)	17 cm	42 cm	66 cm	91 cm	116 cm	140 cm
15	7.0	10.54	10.88	11.51	11.90		10.25
	9.0	10.95	11.01	11.21	12.83		12.11
	12.0	10.65	11.09	11.29	13.11		14.43
	15.0	10.89	11.18	11.53	12.91		16.14
20	7.0	10.80	11.06	11.26	13.05		13.16
	9.0	10.98	11.33	11.72	13.59		15.11
	12.0	10.77	11.34	11.91	12.32		15.35
	15.0	10.78	11.52	12.20	12.77		14.41
25	9.0	10.75	11.55	12.23	13.36		15.29
	12.0	10.98	11.79	12.70	13.87		15.57
	15.0	11.09	12.06	12.93	13.66		15.88
30	9.0	11.37	12.40	12.94	14.54	15.11	16.65
	12.0	11.09	12.32	13.21	14.83		16.80
	15.0	11.82	12.58	13.55	14.95	15.40	16.98
35	9.0	12.07	13.29	14.10	15.00		18.08
	12.0	11.88	13.20	13.90	15.70	17.06	18.13
	15.0	12.02	13.12	13.89	15.70		18.23

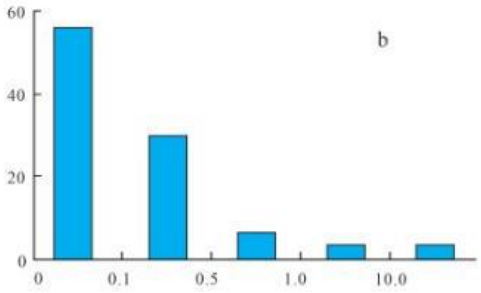

Fig. 4 The RQD histogram and comprehensive statistics

1. Establish RQD state diagram P*Q matrix to measure RQD breakdown area and uncertainty
2. Convert RQD into cohesive force and internal contact angle, and perform P*Q quantitative mapping
3. For P*Q, use the Bishop End method to calculate the safety factor of the plate.
4. Calculate the safety factor and failure probability distribution function

Before we apply the given uncertainty or unmeasured criterion to demonstrate the stability analysis, the analysis was validated in the following experiments. It is consistent with the case study and demonstrates the feasibility of the method on a given rock structure affected by external forces . Subsequently, camera T1 observed various classified events in the upstream section between 14:00 and 16:00. Rain station information shows that the rainfall in the area was 8 mm per hour from 14:00 to 16:00 that day. At that time, the cumulative rainfall in the basin was 18 mm (Fig. 3(a)). The first real rainfall amount reached 100 mm, and the first wave of events occurred on 14.43.45. Because the images captured by the T1 camera are affected by sunlight reflection, they cannot be clearly observed. The left and right lateral flow phenomena can be observed simultaneously. Through the footage captured by the T5 camera before and after the accident, it was observed that the accident on that day caused serious blockage of the merged channel, and vegetation was observed on the right side of the image of the original channel (2b). At 13:43:45 rocks are faintly visible moving downstream, forming the first wave event of the day. Imaging data indicate that the depth is less than half of the lateral storage volume. At approximately 14:16:05, camera T1 observed the ground flowing into the shooting channel (Fig. 3(c)). The flow course and magnitude of this wave are similar to those of the first wave. Through the camera image at this time, it was observed that the front was composed of gravel, but due to the influence of sunlight reflection and the accumulation of the left bank embankment, the subsequent situation could not be observed. At 14:35 minutes and 25 seconds, the range from the cliff observed by the camera to the shooting screen (Fig. 3(d)), excluding the recording screen at this time, it is observed that the end of the wave front is mainly composed of gravel, and then fully developed (Fig. 3(e)). In addition, this wave is larger than the previous two waves and is about half the depth of the sidewall. After the passage of the third wave, camera T1 observed continued downward movement after the event. The fourth wave was observed downstream at 14:37:45 (Fig. 3(f)), and the next wave lasted until approximately 14:37:45. 14:45. Overall, the upstream segment experienced four events. In the difference map before and after the event, it can be observed that the slightly curved and concave width of the upper reaches was strongly eroded (Fig. 3(g)). In addition, the right bank of the ditch is also affected by bank accumulation. Since the reversing section camera T2 and the mid-section camera T3 lack image data, the images

Table 2 Values of Mohr-Coulomb cohesion and friction

Unit Weight(kN/m3) and Angle of Internal Friction (deg)							
Cohesion (KPa)		Friction (deg)		Designation		Normal and shear	
σt(PA)	εp	σt(PA)	εp	σt(PA)	εp	σt(PA)	εp
176780000	0	150000000	0	125000000	0	100000000	0
192941000	0.003071	167500000	0.003325	143750000	0.003563	120000000	0.0038
217941000	0.007821	192500000	0.008075	168750000	0.008313	145000000	0.00855
242941000	0.012571	217500000	0.012825	193750000	0.013063	170000000	0.0133
267941000	0.017321	242500000	0.017575	218750000	0.017813	195000000	0.01805
292941000	0.022071	267500000	0.022325	243750000	0.022563	220000000	0.0228
317941000	0.026821	292500000	0.027075	268750000	0.027313	245000000	0.02755
342941000	0.031571	317500000	0.031825	293750000	0.032063	270000000	0.0323
367941000	0.036321	342500000	0.036575	318750000	0.036813	295000000	0.03705
392941000	0.041071	367500000	0.041325	343750000	0.041563	320000000	0.0418
417941000	0.045821	392500000	0.046075	368750000	0.046313	345000000	0.04655
442941000	0.050571	417500000	0.050825	393750000	0.051063	370000000	0.0513
467941000	0.055321	442500000	0.055575	418750000	0.055813	395000000	0.05605
492941000	0.060071	467500000	0.060325	443750000	0.060563	420000000	0.0608
517941000	0.064821	492500000	0.065075	468750000	0.065313	445000000	0.06555
542941000	0.069571	517500000	0.069825	493750000	0.070063	470000000	0.0703
567941000	0.074321	542500000	0.074575	518750000	0.074813	495000000	0.07505
592941000	0.079071	567500000	0.079325	543750000	0.079563	520000000	0.0798
617941000	0.083821	592500000	0.084075	568750000	0.084313	545000000	0.08455
642941000	0.088571	617500000	0.088825	593750000	0.089063	570000000	0.0893
667941000	0.093321	642500000	0.093575	618750000	0.093813	595000000	0.09405
692941000	0.098071	667500000	0.098325	643750000	0.098563	620000000	0.0988
717941000	0.102821	692500000	0.103075	668750000	0.103313	645000000	0.10355
742941000	0.107571	717500000	0.107825	693750000	0.108063	670000000	0.1083
767941000	0.112321	742500000	0.112575	718750000	0.112813	695000000	0.11305
792941000	0.117071	767500000	0.117325	743750000	0.117563	720000000	0.1178
817941000	0.121821	792500000	0.122075	768750000	0.122313	745000000	0.12255
842941000	0.126571	817500000	0.126825	793750000	0.127063	770000000	0.1273
867941000	0.131321	842500000	0.131575	818750000	0.131813	795000000	0.13205
892941000	0.136071	867500000	0.136325	843750000	0.136563	820000000	0.1368
917941000	0.140821	892500000	0.141075	868750000	0.141313	845000000	0.14155
942941000	0.145571	917500000	0.145825	893750000	0.146063	870000000	0.1463
967941000	0.150321	942500000	0.150575	918750000	0.150813	895000000	0.15105
992941000	0.155071	967500000	0.155325	943750000	0.155563	920000000	0.1558
1017941000	0.159821	992500000	0.160075	968750000	0.160313	945000000	0.16055
1042941000	0.164571	1017500000	0.164825	993750000	0.165063	970000000	0.1653
1067941000	0.169321	1042500000	0.169575	1018750000	0.169813	995000000	0.17005
1092941000	0.174071	1067500000	0.174325	1043750000	0.174563	1020000000	0.1748
1117941000	0.178821	1092500000	0.179075	1068750000	0.179313	1045000000	0.17955
1142941000	0.183571	1117500000	0.183825	1093750000	0.184063	1070000000	0.1843
1167941000	0.188321	1142500000	0.188575	1118750000	0.188813	1095000000	0.18905
1192941000	0.193071	1167500000	0.193325	1143750000	0.193563	1120000000	0.1938
1217941000	0.197821	1192500000	0.198075	1168750000	0.198313	1145000000	0.19855

captured by the convergence section camera T4 and the convergence section camera T5 are greatly affected by sunlight reflection. Therefore, this study uses the T6 camera on the downstream section to record the sequence of events passing through the downstream section. Explain the differences in the structural classification of Qishan.

After the simulation is completed, the method in Section 2.2 is applied to obtain the safety factor of the gradient stability analysis of the RQD diagram using the general main diagram and simulation diagram . For safety reasons,

three different slopes were considered. Table 1 shows the safety factors calculated from the overall data, as well as the maximum, minimum and average safety factors obtained from the simulation plots. Table 1 shows that the average reliability coefficients of the simulated plots are close to the detailed complete data. A symmetric matrix or the corresponding symmetric term in a symmetric term is a symmetric matrix, for example

$$\begin{bmatrix} M_{11} & M_{12} \\ \star & M_{22} \end{bmatrix} + M_1^T M \star + (M_2 + \star)$$
$$= \begin{bmatrix} M_{11} & M_{12} \\ M_{12}^T & M_{22} \end{bmatrix} + M_1^T M M_1 + (M_2 + M_2^T).$$

Represents the sum of weights of several submatrices, for example

$$M_\mu = \sum_{i=1}^{n} \mu_i M_i$$
$$M_{\mu\mu} = \sum_{i=1}^{n} \sum_{j=1}^{n} \mu_i \mu_j M_{ij}$$

where μi represents the weight of Mi in Mμ , gradient $\mu_i \geq 0$且$\sum_{i=1}^{n} \mu_i = 1$.vector the gradient of a scalar function $f(x) \in R$is $x \in R^n$a vector with dimension order n×1, for example

$$\nabla_x f(x) = \begin{bmatrix} \frac{\partial f}{\partial x_1} \\ \frac{\partial f}{\partial x_2} \\ \vdots \\ \frac{\partial f}{\partial x_n} \end{bmatrix} = \frac{\partial f}{\partial x}$$

Hessian matrix : The Hessian matrix of a function $x \in R^n$is $f(x) \in R$an n×n matrix , for example

$$\nabla_{xx} f(x) = \begin{bmatrix} \frac{\partial^2 f}{\partial x_1^{\ 2}} & \frac{\partial^2 f}{\partial x_1 \partial x_2} & \cdots & \frac{\partial^2 f}{\partial x_1 \partial x_n} \\ \frac{\partial^2 f}{\partial x_2 \partial x_1} & \frac{\partial^2 f}{\partial x_2^{\ 2}} & \cdots & \frac{\partial^2 f}{\partial x_2 \partial x_n} \\ \vdots & \ddots & \ddots & \vdots \\ \frac{\partial^2 f}{\partial x_n \partial x_1} & \cdots & \cdots & \frac{\partial^2 f}{\partial x_n^{\ 2}} \end{bmatrix}$$

4. Case description

Survey data include RQD measurements from 27 mine sites within the Alaska Gold Exploration Program. The area was assessed as part of a feasibility in this study for the open-pit field mine project. Preliminary studies formed the geological and geotechnical basis of this study. As with other field mining projects in the area, the rock deposits are located primarily in quartz veins associated peculiarly with intrusive veins. The mine is located in a geological complex of sedimentary and volcanic rocks. Preliminary investigations have identified six major lithological units. During the stretching process, rocks will undergo various deformations such as settlement, compression, burial, and collapse. This deformation produces highly fragmented rocks of low to moderate strength. The only information currently available to researchers is the lithology of the test holes and the RQD database. The authors acknowledge the limitations of using RQD values to assess slope stability. This article outlines several existing and interrelated challenges about rock structure theory that make it not easy to provide a generally applicable and effective standard operation procedure for numerical inversion in rock stability analytical mechanics. Perhaps the greatest challenge going forward would be finding ways to integrate the spirit of reliable and adaptive modeling into semi-automated analysis processes for inversion. This could be ultimately including further information on how error-tried functions can be designed flexibly and reliably to combine different data sources and soft constraints, and to definitely better deal with limitations and non-uniqueness in material models. It will require the time and funding in the ongoing research to have breakthrough.

5. Experimental results and discussion

5.1 Numerical data analysis

Data are collected every 1.5 meters for statistical analysis. This gap length was chosen to preserve the error and variability of the RQD data and to provide a large enough sample of neighbors for interpolation. A large number of composite samples were prepared for failure simulation and RQD. The RQD histogram and complete data are shown in Fig. 4. We are interested in the real phenomenon of engineering structural parameters of rocks. Upon closer inspection, the high frequency of zero or near-zero RQD can be clarified by: (1) weak rocks in the outcrop, (2) brittle rocks with complex shown fault zones, and (3) generally weaker rocks

The stone is of medium durability and has been damaged and worn. In Fig. 5, the experiment is divided into 4 groups, with a total of 16 models. Since the purpose of this test is to observe the dynamic response of structural materials entering the plastic part, to ensure that the material enters the plastic part, we also use 7.5 times stability control for analysis.

After completing the ABAQUS analysis work, we used the structural stability analysis method to calculate the modal parameters. First, plot the spectrum of the captured top and bottom acceleration duration data and divide to obtain the time-frequency domain gain functions AFm and AFf. Next, we extract the modal information to be calculated from the time-integrated edge spectrum of the normalized time-frequency domain gain function AFf , and then calculate its integrity index II and nonlinearity index NI.

Fig. 6 shows that the scales of Geo1_Y and Geo1_X are quite different from the scales of other axes, and there is no obvious fluctuation in the signal; this section mainly uses the other four axes for spectral analysis. After a quick conversion, observe the reaction of each axis in the results.

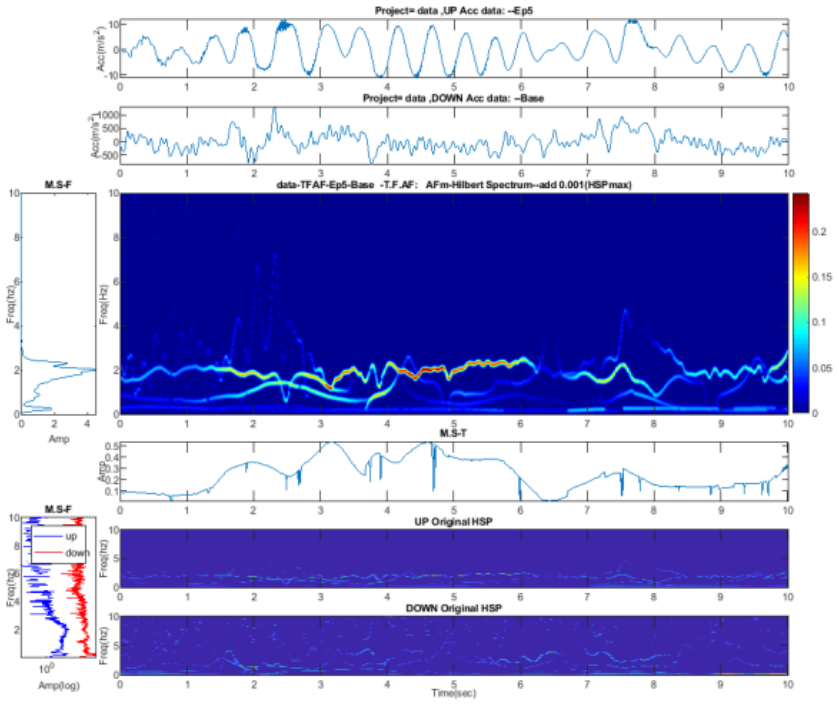

Fig. 5 The experiment was divided into 4 groups with a total of 16 models

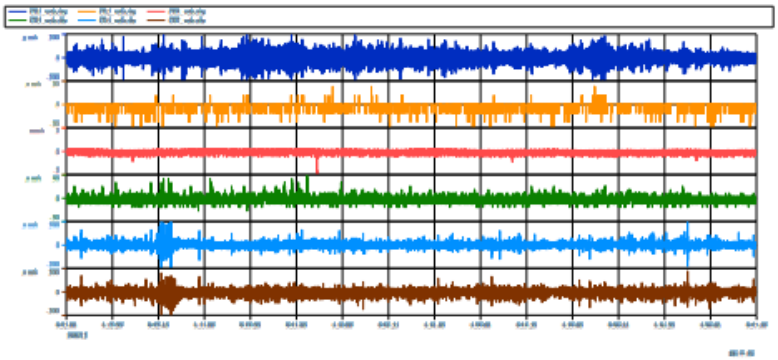

Fig. 6 RQD frequency test by stability theorem of rock structure

The fundamental frequency is different. Among them, the Geo1_Z axis reflects the fundamental frequency of earth-rock flow between 15 and 45 Hz, the Geo2_Z axis is approximately between 15 and 25 Hz, the Geo2_Y axis is approximately between 15 and 40 Hz, and the Geo2_X axis is between 15 and 31_Z and the Geo2_Z axis. To define the fundamental frequency, you must for example define the maximum energy at five points on that axis, and define the fundamental frequency as a frequency range greater than 1/2 times the average energy.

5.2 Crowded and poorly designed

The overburden model is based on lithological records from the exploration drillhole data set. Dimensions for high-performance models. Solid material extends between the highest and lowest levels of each well platform and to levels north and east of where the block is formed. The robust model was developed without considering uncertainties and assuming that the loads are continuous layers.

SGeMS models fault zones through sequential simulation . Attribution of "errors" and "imperfections" in synthetic data also depends on lithological evidence. In the simulation, damaged stones are classified as category 1 and undamaged stones are classified as category 0. In the aggregate data, 89% of the stones were classified as 0 (thrown stones) and 11% were classified as 1 (thrown stones).

Experimental changes in indicator data are calculated and entered into the model. Figure 7 shows the experimental contours. In some experiments, the lower edge of the comparison graph is relatively smooth at the beginning of the experiment and gradually becomes jagged as the experiment proceeds, such as C and D. What these

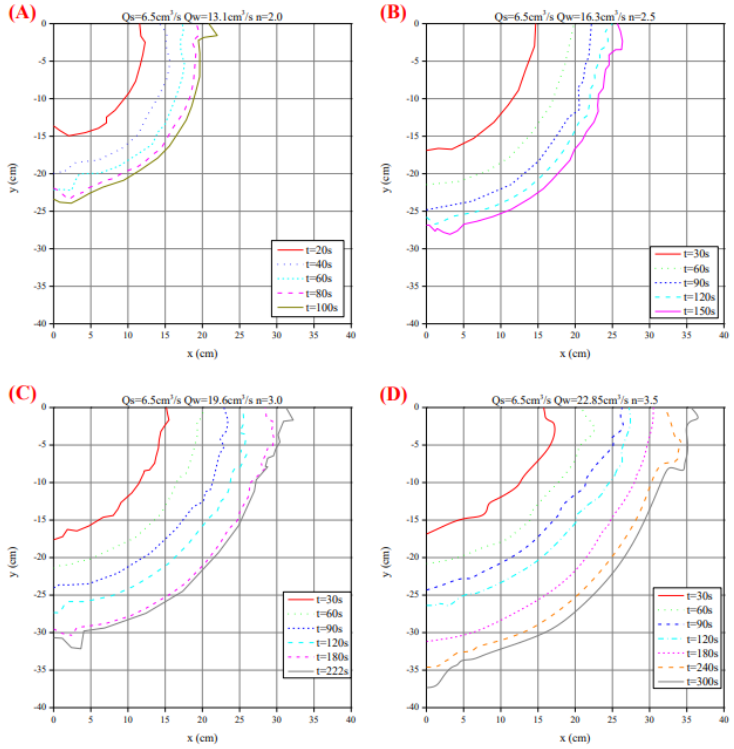

Fig. 7 Planar stacking profile of Q_S=6.5 cm^3/*s* (n=2.0~3.5) (a) n=2.0,Q_W=13.1 cm^3/*s*, (b) n=2.5, Q_W=16.3 cm^3/*s*, (c) n=3.0, Q_W=19.6 cm^3/*s* and (d) n= 3.5Q_W=22.6 cm^3/*s*

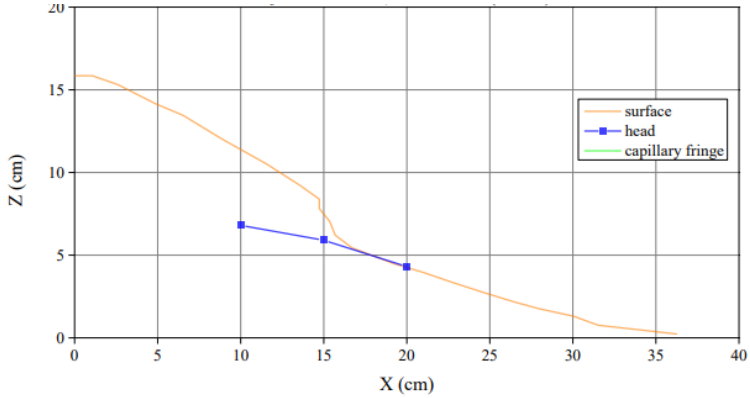

Fig. 8 stability analysis of rock under experiments

experimental cases have in common is that they all undergo rapid change. . When rocks are in a steady state of laminar flow, sediments fall evenly. Once stabilized, sediments fall only at the edges, gradually forming irregular edges as they change course.

In the case of Q_w =20.9 cm^3/s , the rough edge after 2400 seconds is not entirely caused by lithification . The lithification at this time can no longer reach the bottom, but what seeps out from the bottom will flow out from the center, accumulating along the way to form the result.

Producing just ten maps increases computer efficiency while producing important statistics from exploratory drilling data. Therefore, SIS is used to generate ten equally likely 3D error maps. According to the geological map contained in the geological map, the fault zone widens and flattens in the north-south direction. Experimental Study. The post-processed fault model retained under 90% of the clean rock and over 10% of the damaged rock.

Compare simulated and aggregated versions of the data to identify error patterns. After the update, over 10% of models were defective. The threshold for 10 error models is approx. 0.1, which is very similar to the preset threshold for complex error regions. Validation results show that the fault map in the simulation preserves the one- and two-dimensional geological characteristics of the fault zone.

5.3 Rock stability quality label

Experimental changes in NST-RQD data were calculated and fitted to the anisotropic orientation model. The height and tolerance to obtain the most continuous waveform are the same parameters specified when

calculating the error waveform. Fig. 8 shows the experimental variogram corresponding to the theoretical variogram. Converting level cards into individual damage cards is very similar. Two maps provide RQD values that only include predictions for very hard, low-grade rock, while the other eight maps provide predictions for very hard, brittle, high-grade rock. The SGeM TRANSCAT tool was used to create average maps of the 10 RQD categories. Scaling preserves the ratio of each RQD category. This article outlines several existing and interrelated challenges about rock structure theory that make it not easy to provide a generally applicable and effective standard operation procedure for numerical inversion in rock stability analytical mechanics. Perhaps the greatest challenge going forward would be finding ways to integrate the spirit of reliable and adaptive modeling into semi-automated analysis processes for inversion. This could be ultimately including further information on how error-tried functions can be designed flexibly and reliably to combine different data sources and soft constraints, and to definitely better deal with limitations and non-uniqueness in material models. It will require the time and funding in the ongoing research to have breakthrough.

5.4 Slope resistance analysis

Gravity tilt analysis is based on layered RQD maps. Rocscience - Slideshow reproducing the geometry of the eastern segment, including outcrop boundaries, bedrock contacts, fault type boundaries, and rock boundaries between RQD property categories. Each disk was cut in five steps at angles ranging shown in examples to study the effect of tilt angle on rock stability. From Table 2, the Mohr-Coulomb theory is generally consistent with RQD, but it should be noted that it is not suitable for this study. Contrary to the previous literature, this analysis specifically only considers surface type rocks and assumes isotropic friction values within each RQD category. It is only used as the basis for each type of rock characteristics in the RQD. It shows the expected scale characteristics for this analysis. Since the data recorded as errors are also numerically measured at or near zero RQD, the expected rock characteristics in fault zones are the same as for many hard rocks.

The sliding surface is established using specific method and automatic search for circular fault planes. Automatic search for boundary conditions uses a simple algorithm to iteratively search for the minimum safety factor for circular defect surfaces. In order to eliminate surface errors, the minimum search radius is 10 m. This analysis assumes that the minimum safety factors. The steeper the slope, the smaller the slope reduction value. Therefore, the research focuses on searching for the steepest slope with a safety factor. It is significant to understand that the results of the stability analysis depend greatly on the location in our analysis. The results suggested relate only to the exact location of the intervertebral disc examined. Additionally, a stability analysis must be performed for each geographic area of the well to calculate the stable inclination angle for the entire well. The purpose of our study is showing how common spatial uncertainties (structural and engineering geotechnical) can be incorporated into rock stability criterion and analysis and applied to field mine slope stability of rock analysis.

6. Conclusions

This study combines geospatial modeling of geological structures and geometric characteristics. Geostatistical modeling plots are used to study the stability of quarry slopes with limited information. The application of geostatic model diagrams for slope stabilization is only one of many possible applications. The generated RQD diagrams can also be used to identify critical areas for slope stability and the most effective stabilization methods (e.g., anchors, bolts, etc.). After receiving raw data from the mine's underground exploration plan, RQDs and structural drawings can be used to measure the center of gravity and design rock reinforcements. Beyond mining, the same technology can be applied to tunnels, highways and other projects that require stability analysis or rock mechanism reinforcement.

These studies demonstrate an interest in the uncertainty and heterogeneity of geological structures and geometric characteristics. This method is suitable for preliminary assessment of slope stability when on-site information is limited. This article outlines several existing and interrelated challenges about rock structure theory that make it not easy to provide a generally applicable and effective standard operation procedure for numerical inversion in rock stability analytical mechanics. Perhaps the greatest challenge going forward would be finding ways to integrate the spirit of reliable and adaptive modeling into semi-automated analysis processes for inversion. This could be ultimately including further information on how error-tried functions can be designed flexibly and reliably to combine different data sources and soft constraints, and to definitely better deal with limitations and non-uniqueness in material models. It will require the time and funding in the ongoing research to have breakthrough. The goals of this paper are towards access to adequate, safe and affordable housing and basic services, promotion of inclusive and sustainable urbanization and participation, implementation of sustainable and disaster-resilient buildings, sustainable human settlement planning and manage. Simulation results of linear and nonlinear structures show that the proposed method is able to identify structural parameters and their changes due to damage and unknown excitations. Therefore, the goal is believed to achieved in the near future by the ongoing development of AI and control theory.

Ethical standards

The authors have no conflicts of interest with respect to the publication of this article. All data and measurements analyzed in this study are included in this article.

Acknowledgments

The authors are grateful for the research grants of GDUPT, Peoples R China under Grant NO. 2019rc098, and the Grant NO. NO. 2021rc002 in Guangdong Province,

Peoples R China. Also, the authors wish to appreciate to constructive suggestions from the anonymous reviewers.

References

Bai, B., Zhou, R., Cai, G., Hu, W. and Yang, G. (2021), "Coupled thermo-hydro-mechanical mechanism in view of the soil particle rearrangement of granular thermodynamics", *Comput. Geotech.*, **137**, 104272. https://doi.org/10.1016/j.compgeo.2021.104272.

Canakci, H., Aziz, A. and Celik, F. (2016), "Soil stabilization of clay with lignin, rice husk powder and ash", *Geomech. Eng*., **8**(1), 67-79. https://doi.org/10.12989/gae.2015.8.1.067.

Cao, J., Bu, F., Wang, J., Bao, C., Chen, W. and Dai, K. (2023), "Reconstruction of full-field dynamic responses for large-scale structures using optimal sensor placement", *J. Sound Vib*., **554**, 117693. https://doi.org/10.1016/j.jsv.2023.117693.

Cao, J., He, H., Zhang, Y., Zhao, W., Yan, Z. and Zhu, H. (2023), "Crack detection in ultrahigh-performance concrete using robust principal component analysis and characteristic evaluation in the frequency domain", *Struct. Health Monit*., https://doi.org/10.1177/14759217231178457.

Cao, J., Quek, S., Xiong, H. and Yang, Z. (2023), "Comparison of constrained unscented and cubature Kalman filters for nonlinear system parameter identification", *J. Eng. Mech*., **149**(11), 4023088. https://doi.org/10.1061/JENMDT.EMENG-7091.

Ceylan, H., Gopalakrishnan, K. and Kim, S. (2019), "Soil stabilization with bioenergy coproduct", *Transp. Res. Record*, **2186**, 130-137. https://doi.org/10.3141/2186-14.

Chang, I., Im, J., Lee, S.K. and Cho, G.C. (2017), "Strength durability of gellan gum biopolymer-treated Korean sand with cyclic wetting and drying", *Constr. Build. Mater*., **143**, 210-221. https://doi.org/10.1016/j.conbuildmat.2017.02.061.

Chen, L., Wang, Z., Li, X. and Gao, L. (2023), "Enhancing the accuracy of the scale of fluctuation estimating for tunnel surrounding rock mass characteristics", *Int. J. Rock Mech. Min. Sci*., 170. https://doi.org/10.1016/j.ijrmms.2023.105513.

Chen, Y., Zhu, L., Hu, Z., Chen, S. and Zheng, X. (2023), "Risk propagation in multilayer heterogeneous network of coupled system of large engineering project", *J. Management Eng*., **38**(3), 4022003. https://doi.org/10.1061/(ASCE)ME.1943-5479.0001022.

Cui, W., Caracoglia, L., Zhao, L. and Ge, Y. (2023), "Examination of occurrence probability of vortex-induced vibration of long-span bridge decks by Fokker–Planck–Kolmogorov equation", *Struct. Saf*., **105**, 102369. https://doi.org/10.1016/j.strusafe.2023.102369.

Cui, W., Zhao, L. and Ge, Y. (2023), "Wind-induced buffeting vibration of long-span bridge considering geometric and aerodynamic nonlinearity based on reduced-order modeling", *J. Struct. Eng*., **149**(11), 4023160. https://doi.org/10.1061/JSENDH.STENG-11543.

Cui, W., Zhao, L., Ge, Y. and Xu, K. (2024), "A generalized van der Pol nonlinear model of vortex-induced vibrations of bridge decks with multistability", *Nonlinear Dynam*., **112**(1), 259-272. https://doi.org/10.1007/s11071-023-09047-9.

Dai, Z., Li, X. and Lan, B. (2023), "Three-dimensional modeling of Tsunami waves triggered by submarine landslides based on the smoothed particle hydrodynamics method", *J. Mar. Sci. Eng*., **11**(10), 2015. https://doi.org/10.3390/jmse11102015.

Du, W. and Wang, G. (2014), "Fully probabilistic seismic displacement analysis of spatially distributed slopes using spatially correlated vector intensity measures", *Earthq. Eng. Struct. D*., **43**(5), 661-679. https://doi.org/10.1002/eqe.2365.

Ham, S.M., Chang, I., Noh, D.H. and Kwon, T.H. (2018), "Improvement of surface erosion resistance of sand by microbial biopolymer formation", *Geotech. Geoenviron. Eng*., **144**(7), 06018004-1-6. https://doi.org/10.1061/(ASCE)GT.1943-5606.0001900.

Han, S., Li, H., Li, M., Zhang, J., Ma, J. and Zhao, W. (2022), "Deep learning–based stochastic modelling and uncertainty analysis of fault networks", *Bull. Eng. Geol. Environ*., **81**, 242. https://doi.org/10.1007/s10064-022-02735-7.

He, H., Shuang, E., Wen, T., Yao, J., Wang, X., He, C. and Yu, Y. (2023), "Employing novel N-doped graphene quantum dots to improve chloride binding of cement", *Constr. Build. Mater*., **401**, 132944. doi: https://doi.org/10.1016/j.conbuildmat.2023.132944

Huang, H., Li, M., Zhang, W. and Yuan, Y. (2022), "Seismic behavior of a friction-type artificial plastic hinge for the precast beam–column connection", *Arch. Civil Mech. Eng*., **22**(4), 201. https://doi.org/10.1007/s43452-022-00526-1.

Huang, H., Yao, Y., Zhang, W. and Zhou, L. (2023), "A push-out test on partially encased composite column with different positions of shear studs", *Eng. Struct*., **289**, 116343. https://doi.org/10.1016/j.engstruct.2023.116343.

Jia, B. and Zhou, G. (2023), "Estimation of global karst carbon sink from 1950s to 2050s using response surface methodology", *Geo-spatial Inform. Sci*., https://doi.org/10.1080/10095020.2023.2165974.

Jia, S., Dai, Z., Zhou, Z., Ling, H., Yang, Z., Qi, L., Wang, Z., Zhang, X., Thanh, H.V. and Soltanian, M.R. (2023), "Upscaling dispersivity for conservative solute transport in naturally fractured media", *Water Res*., **235**, 119844. https://doi.org/10.1016/j.watres.2023.119844.

Johari, A. and Fooladi, H. (2023), "System reliability analysis of site slope using the conditional spatial variability of soil characteristics", *Iran J. Sci. Technol. Trans. Civ. Eng*., https://doi.org/10.1007/s40996-023-01200-z.

Kring, K. and Chatterjee, S. (2020), "Uncertainty quantification of structural and geotechnical parameter by geostatistical simulations applied to a stability analysis case study with limited exploration data", *Int. J. Rock Mech. Min. Sci*., **125**. https://doi.org/10.1016/j.ijrmms.2019.104157.

Li, D., Nie, J., Wang, H. and Ren, W. (2024), "Loading condition monitoring of high-strength bolt connections based on physics-guided deep learning of acoustic emission data", *Mech. Syst. Signal Pr*., **206**, 110908. https://doi.org/10.1016/j.ymssp.2023.110908.

Li, J., Chen, M. and Li, Z. (2022), "Improved soil–structure interaction model considering time-lag effect", *Comput. Geotech*., **148**, 104835. https://doi.org/10.1016/j.compgeo.2022.104835.

Li, J., Liu, Y. and Lin, G. (2023), "Implementation of a coupled FEM-SBFEM for soil-structure interaction analysis of large-scale 3D base-isolated nuclear structures", *Comput. Geotech*., **162**, 105669. https://doi.org/10.1016/j.compgeo.2023.105669.

Li, J., Zhang, Y., Lin, L. and Zhou, Y. (2023), "Study on the shear mechanics of gas hydrate-bearing sand-well interface with different roughness and dissociation", *Bull. Eng. Geol. Environ*., **82**(11), 404. https://doi.org/10.1007/s10064-023-03432-9.

Li, X., Zhu, H. and Yuan, Q. (2023), "Dilatancy equation based on the property-dependent plastic potential theory for geomaterials", *Fractal and Fractional*, **7**(11), 824. https://doi.org/10.3390/fractalfract7110824.

Liu, C., Cui, J., Zhang, Z., Liu, H., Huang, X. and Zhang, C. (2021), "The role of TBM asymmetric tail-grouting on surface settlement in coarse-grained soils of urban area: Field tests and FEA modelling", *Tunn. Undergr. Sp. Tech*., **111**, 103857. https://doi.org/10.1016/j.tust.2021.103857.

Liu, W., Liang, J. and Xu, T. (2023), "Tunnelling-induced ground deformation subjected to the behavior of tail grouting materials", *Tunn. Undergr. Sp. Tech*., **140**, 105253.

https://doi.org/10.1016/j.tust.2023.105253.

Liu, W., Zhou, H., Zhang, S. and Zhao, C. (2023), "Variable parameter creep model based on the separation of viscoelastic and viscoplastic deformations", *Rock Mech. Rock Eng.*, **56**(6), 4629-4645. https://doi.org/10.1007/s00603-023-03266-7.

Long, X., Mao, M., Su, T., Su, Y. and Tian, M. (2023), "Machine learning method to predict dynamic compressive response of concrete-like material at high strain rates", *Defence Tech.*, **23**, 100-111. https://doi.org/10.1016/j.dt.2022.02.003.

Ren, C., Yu, J., Liu, S., Yao, W., Zhu, Y. and Liu, X. (2022), "A plastic strain-induced damage model of porous rock suitable for different stress paths", *Rock Mech. Rock Eng.*, **55**(4), 1887-1906. https://doi.org/10.1007/s00603-022-02775-1.

Ren, C., Yu, J., Liu, X., Zhang, Z. and Cai, Y. (2022), "Cyclic constitutive equations of rock with coupled damage induced by compaction and cracking", *Int. J. Min. Sci. Tech.*, **32**(5), 1153-1165. https://doi.org/10.1016/j.ijmst.2022.06.010

Ren, C., Yu, J., Zhang, C., Liu, X., Zhu, Y. and Yao, W. (2023), "Micro–macro approach of anisotropic damage: A semi-analytical constitutive model of porous cracked rock", *Eng. Fract. Mech.*, **290**, 109483. https://doi.org/10.1016/j.engfracmech.2023.109483.

She, A., Wang, L., Peng, Y. and Li, J. (2023), "Structural reliability analysis based on improved wolf pack algorithm AK-SS", *Structures*, **57**, 105289. https://doi.org/10.1016/j.istruc.2023.105289.

Shi, M., Hu, W., Li, M., Zhang, J., Song, X. and Sun, W. (2023). "Ensemble regression based on polynomial regression-based decision tree and its application in the in-situ data of tunnel boring machine", *Mech. Syst. Signal Pr.*, **188**, 110022. https://doi.org/10.1016/j.ymssp.2022.110022.

Shi, M., Lv, L. and Xu, L. (2023), "A multi-fidelity surrogate model based on extreme support vector regression: fusing different fidelity data for engineering design", *Eng. Comput.*, **40**(2), 473-493. https://doi.org/10.1108/EC-10-2021-0583.

Stavropoulou, M., Exadakytlos, G. and Saratsis, G. (2022), "A combined three-dimensional geological-geostatistical-numerical model of underground excavations in rock", *Rock Mech. Rock Eng.*, 213-243.

Suchomel, R. and Masin, D. (2022), "Comparison of different probabilistic methods for predicting stability of a slope in spatially variable c-φ soil", *Comput. Geotech.*, **37**(1-2), 132-140. https://doi.org/10.1016/j.compgeo.2009.08.005.

Sung, E. (2018), "Probabilistic stability analyses of slopes using the ANN-based response surface", *Comput. Geotech.*, **36**(5), 787-797. https://doi.org/10.1016/j.compgeo.2009.01.003.

Tian, H., Pei, J., Huang, J., Li, X., Wang, J., Zhou, B. and Wang, L. (2020), "Garlic and winter wheat identification based on active and passive satellite imagery and the google earth engine in Northern China", *Remote Sens.* (Basel, Switzerland), **12**, 3539. https://doi.org/10.3390/rs12213539.

Wang, X., Li, L., Xiang, Y., Wu, Y. and Wei, M. (2024), "The influence of basalt fiber on the mechanical performance of concrete-filled steel tube short columns under axial compression", *Front. Mater.*, 10. https://doi.org/10.3389/fmats.2023.1332269.

Xu, J., Zhou, G., Su, S., Cao, Q. and Tian, Z. (2022), "The development of a rigorous model for bathymetric mapping from multispectral satellite-images", *Remote Sens.*, **14**(10). https://doi.org/10.3390/rs14102495.

Xu, Z., Li, X., Li, J., Xue, Y., Jiang, S., Liu, L. and Sun, Q. (2022), "Characteristics of source rocks and genetic origins of natural gas in deep formations, Gudian Depression, Songliao Basin, NE China", *ACS Earth and Space Chemistry*, **6**(7), 1750-1771. https://doi.org/10.1021/acsearthspacechem.2c00065

Xu, P., Lan, D., Wang, F. and Shin, I. (2023), "In-memory computing integrated structure circuit based on nonvolatile flash memory unit", *Electronics*, **12**(14), 3155. https://doi.org/10.3390/electronics12143155.

Xu, Y., Wang, E., Yang, Y. and Chang, Y. (2022), "A unified collaborative representation learning for neural-network based recommender systems", *IEEE T. Knowledge Data Eng.*, **34**(11), 5126-5139. https://doi.org/10.1109/TKDE.2021.3054782.

Yan, T., Xu, R., Sun, S.H., Hou, Z.K. and Feng, J.Y. (2023), "A real-time intelligent lithology identification method based on a dynamic felling strategy weighted random forest algorithm", *Petroleum Sci.*, https://doi.org/10.1016/j.petsci.2023.09.011.

Yang, L., Wang, H., Xu, H., Guo, D. and Li, M. (2023, "Experimental study on characteristics of water imbibition and ion diffusion in shale reservoirs", *Geoenergy Sci. Eng.*, **229**, 212167. https://doi.org/10.1016/j.geoen.2023.212167.

Yang, L., Yang, D., Zhang, M., Meng, S., Wang, S., Su, Y.,... Xu Long. (2024). Application of nano-scratch technology to identify continental shale mineral composition and distribution length of bedding interfacial transition zone - A case study of Cretaceous Qingshankou formation in Gulong Depression, Songliao Basin, NE China. Geoenergy Science and Engineering, 234, 212674. doi: https://doi.org/10.1016/j.geoen.2024.212674

Yao, W., Yu, J., Liu, X., Zhang, Z., Feng, X. and Cai, Y. (2023), "Experimental and theoretical investigation of coupled damage of rock under combined disturbance", *Int. J. Rock Mech. Min. Sci.*, **164**, 105355. https://doi.org/10.1016/j.ijrmms.2023.105355

Yin, H., Wu, Q., Yin, S., Dong, S., Dai, Z. and Soltanian, M.R. (2023), "Predicting mine water inrush accidents based on water level anomalies of borehole groups using long short-term memory and isolation forest", *J. Hydrology*, **616**, 128813. https://doi.org/10.1016/j.jhydrol.2022.128813.

Yin, L., Wang, L., Li, J., Lu, S., Tian, J., Yin, Z. and Zheng, W. (2023), "YOLOV4_CSPBi: Enhanced land target detection model", *Land*, **12**(9), 1813. https://doi.org/10.3390/land12091813.

Yu, J., Zhu, Y., Yao, W., Liu, X., Ren, C., Cai, Y. and Tang, X. (2021), "Stress relaxation behaviour of marble under cyclic weak disturbance and confining pressures", *Measurement*, **182**, 109777. https://doi.org/10.1016/j.measurement.2021.109777.

Zhang, J. and Zhang, C. (2023), "Using viscoelastic materials to mitigate earthquake-induced pounding between adjacent frames with unequal height considering soil-structure interactions", *Soil Dyn. Earthq. Eng.*, **172**, 107988. https://doi.org/10.1016/j.soildyn.2023.107988.

Zhang, X., Wang, S., Liu, H., Cui, J., Liu, C. and Meng, X. (2024), "Assessing the impact of inertial load on the buckling behavior of piles with large slenderness ratios in liquefiable deposits", *Soil Dyn. Earthq. Eng.*, **176**, 108322. https://doi.org/10.1016/j.soildyn.2023.108322.

Zhou, G., Su, S., Xu, J., Tian, Z. and Cao, Q. (2023), "Bathymetry retrieval from spaceborne multispectral subsurface reflectance", *IEEE J. Selec.Topics Appl. Earth Observ. Remote Sens.*, **16**, 2547-2558. https://doi.org/10.1109/JSTARS.2023.3249789.

CC